**DIGITAL ACCESS TO
SCHOLARSHIP AT HARVARD**

DASH.HARVARD.EDU

HARVARD LIBRARY
Office for Scholarly Communication

PS1-14bj: A Hydrogen-poor Superluminous Supernova with a Long Rise and Slow Decay.

The Harvard community has made this article openly available. Please share how this access benefits you. Your story matters

PS1-14BJ: A HYDROGEN-POOR SUPERLUMINOUS SUPERNOVA WITH A LONG RISE AND SLOW DECAY

R. Lunnan[1,2], R. Chornock[3], E. Berger[2], D. Milisavljevic[2], D. O. Jones[4], A. Rest[5], W. Fong[6,18], C. Fransson[7], R. Margutti[8], M. R. Drout[2], P. K. Blanchard[2], P. Challis[2], P. S. Cowperthwaite[2], R. J. Foley[9,10,11], R. P. Kirshner[2], N. Morrell[12], A. G. Riess[5,4], K. C. Roth[13], D. Scolnic[14], S. J. Smartt[15], K. W. Smith[15], V. A. Villar[2], K. C. Chambers[16], P. W. Draper[17], M. E. Huber[16], N. Kaiser[16], R.-P. Kudritzki[16], E. A. Magnier[16], N. Metcalfe[17], and C. Waters[16]

ApJ in press

ABSTRACT

We present photometry and spectroscopy of PS1-14bj, a hydrogen-poor superluminous supernova (SLSN) at redshift $z = 0.5215$ discovered in the last months of the Pan-STARRS1 Medium Deep Survey. PS1-14bj stands out by its extremely slow evolution, with an observed rise of $\gtrsim 125$ rest-frame days, and exponential decline out to ~ 250 days past peak at a measured rate of 0.01 mag day^{-1}, consistent with fully-trapped ^{56}Co decay. This is the longest rise time measured in a SLSN to date, and the first SLSN to show a rise time consistent with pair-instability supernova (PISN) models. Compared to other slowly-evolving SLSNe, it is spectroscopically similar to the prototype SN 2007bi at maximum light, though lower in luminosity ($L_{\mathrm{peak}} \simeq 4.6 \times 10^{43}$ erg s^{-1}) and with a flatter peak than previous events. PS1-14bj shows a number of peculiar properties, including a near-constant color temperature for > 200 days past peak, and strong emission lines from [O III] λ5007 and [O III] λ4363 with a velocity width of $\sim$3400 km s^{-1} in its late-time spectra. These both suggest there is a sustained source of heating over very long timescales, and are incompatible with a simple ^{56}Ni-powered/PISN interpretation. A modified magnetar model including emission leakage at late times can reproduce the light curve, in which case the blue continuum and [O III] features are interpreted as material heated and ionized by the inner pulsar wind nebula becoming visible at late times. Alternatively, the late-time heating could be due to interaction with a shell of H-poor circumstellar material.

Subject headings: supernovae: general; supernovae: individual (PS1-14bj, LSQ14an)

1. INTRODUCTION

rlunnan@astro.caltech.edu
[1] Department of Astronomy, California Institute of Technology, 1200 East California Boulevard, Pasadena, CA 91125, USA
[2] Harvard-Smithsonian Center for Astrophysics, 60 Garden St., Cambridge, MA 02138, USA
[3] Astrophysical Institute, Department of Physics and Astronomy, 251B Clippinger Lab, Ohio University, Athens, OH 45701, USA
[4] Department of Physics and Astronomy, Johns Hopkins University, 3400 North Charles Street, Baltimore, MD 21218, USA
[5] Space Telescope Science Institute, 3700 San Martin Drive, Baltimore, MD 21218, USA
[6] Steward Observatory, University of Arizona, 933 North Cherry Avenue, Tucson, AZ 85721, USA
[7] The Oskar Klein Centre & Department of Astronomy, Stockholm University, AlbaNova, SE-106 91 Stockholm, Sweden
[8] New York University, Physics department, 4 Washington Place, New York, NY 10003, USA
[9] Department of Astronomy and Astrophysics, University of California, Santa Cruz, CA 95064, USA
[10] Astronomy Department, University of Illinois at Urbana-Champaign, 1002 W. Green Street, Urbana, IL 61801, USA
[11] Department of Physics, University of Illinois at Urbana-Champaign, 1110 W. Green Street, Urbana, IL 61801, USA
[12] Las Campanas Observatory, Carnegie Observatories, Casilla 601, La Serena, Chile
[13] Gemini Observatory, 670 North Aohoku Place, Hilo, HI 96720, USA
[14] Department of Physics, The University of Chicago, Chicago,IL 60637
[15] Astrophysics Research Centre, School of Mathematics and Physics, Queen's University Belfast, Belfast BT7 1NN, UK
[16] Institute for Astronomy, University of Hawaii at Manoa, Honolulu, HI 96822, USA
[17] Department of Physics, Durham University, South Road, Durham DH1 3LE, UK
[18] Einstein Fellow

Superluminous supernovae (SLSNe), characterized by peak luminosities 10-100 times higher than ordinary core-collapse and Type Ia SNe, are a rare type of transients discovered in untargeted surveys over the past decade. Their extreme energetics cannot be explained by the same mechanism as ordinary SNe, requiring either an additional energy source beyond ^{56}Ni decay, or an exotic explosion mechanism. From an observational point of view, SLSNe can be classified into at least two distinct categories (Gal-Yam 2012): H-rich SLSNe ('SLSN-II') show Balmer lines in their spectra, and most are similar to Type IIn SNe and likely indicating strong interaction with circumstellar material (CSM) (e.g., Ofek et al. 2007; Smith et al. 2007, 2010; Rest et al. 2011). In this case, a large fraction of the kinetic energy of the ejecta can be converted into radiation, powering the large luminosities.

In contrast, H-poor SLSNe ('SLSN-I') typically have spectra distinct from any other known SN types, characterized by a very blue continuum with a few, broad features from intermediate-mass elements (e.g., Quimby et al. 2011; Chomiuk et al. 2011; Mazzali et al. 2016). The primary power source for this class is debated: CSM interaction can explain the energetics, but would require several solar masses of H-poor material shed in the last few years to decades before explosion (Chevalier & Irwin 2011; Ginzburg & Balberg 2012; Chatzopoulos & Wheeler 2012b; Moriya et al. 2013). An alternative scenario is energy injection from a central engine, such as the spin-down of a newborn magnetar (Kasen & Bildsten 2010; Woosley 2010; Dessart et al.

2012). ^{56}Ni decay, which powers the optical light curve of ordinary type Ibc SNe, can generally be ruled out for this subclass as the fast timescales at peak are incompatible with the large Ni masses that would be required to power the luminosities (e.g., Quimby et al. 2011; Chomiuk et al. 2011; Lunnan et al. 2013; Inserra et al. 2013).

However, some H-poor SLSNe do show slow decay rates that match that of radioactive ^{56}Co. Gal-Yam (2012) proposed that these be grouped into a third subclass, 'SLSN-R' (the 'R' stands for radioactivity), modeled on the unusual H-poor SLSN SN 2007bi (Gal-Yam et al. 2009; Young et al. 2010). SN 2007bi had both a slow decay rate and a nebular phase spectrum consistent with several solar masses of ^{56}Ni produced in the explosion, leading Gal-Yam et al. (2009) to propose that SN 2007bi was a pair-instability supernova (PISN). This mechanism is theorized to be the final fate of stars with initial masses $140\ M_\odot \lesssim M \lesssim 250\ M_\odot$, where the high temperatures in the oxygen core leads to electron-positron pair production triggering a nuclear explosion (Barkat et al. 1967). While originally thought to be mainly relevant for Population III stars in the early universe (Woosley et al. 2007), models including rotation are able to produce PISNe also from non-zero metallicity stars (Chatzopoulos & Wheeler 2012a; Yusof et al. 2013; Marchant et al. 2016).

The interpretation of SN 2007bi as a PISN (and by extension, the interpretation of 'SLSN-R' as a separate class from other H-poor SLSNe and powered by radioactivity) is controversial, however. A key prediction of PISN models is a long ($\gtrsim 100$ days) rise-time due to the large ejecta mass, which in turn leads to a long diffusion time through the ejecta. As SN 2007bi was discovered near peak, the rise was not observed, and CSM interaction or magnetar spin-down models can also fit the observed light curve. In addition, other H-poor SLSNe with decay rates and spectroscopic properties similar to SN 2007bi have since been discovered, showing shorter rise times incompatible with PISN models but well-fit by magnetar spin-down models (Nicholl et al. 2013), thus casting doubt also on the nature of SN 2007bi. Finding more slowly-evolving SLSNe with well-sampled light curves is therefore crucial in shedding light on the origins of this potential subclass.

Here, we present the discovery and analysis of PS1-14bj, a slowly evolving H-poor SLSN discovered by the Pan-STARRS Medium Deep Survey (PS1/MDS). The photometry and spectroscopic observations are presented in Section 2. We analyze the light curves, including the color evolution and blackbody fits, and use this data to construct a bolometric light curve and estimate the total radiated energy in Section 3. Our spectroscopic sequence, ranging from -51 to $+202$ days relative to peak light, is discussed in Section 4. We discuss the host galaxy properties in Section 5. Section 6 discusses our observations in the context of different models for powering SLSNe, and we summarize our conclusions in Section 7. All calculations in this paper assume a ΛCDM cosmology with $H_0 = 70$ km s^{-1} Mpc^{-1}, $\Omega_M = 0.27$ and $\Omega_\Lambda = 0.73$ (Komatsu et al. 2011).

2. OBSERVATIONS

2.1. *Pan-STARRS1 Summary and Photometry*

The PS1 telescope on Haleakala is a high-étendue wide-field survey instrument, with a 1.8 m diameter primary mirror and a 3.3° diameter field of view, imaged by an array of sixty 4800×4800 pixel detectors with a pixel scale of $0.258''$ (Kaiser et al. 2010; Tonry & Onaka 2009). The $g_{P1}r_{P1}i_{P1}z_{P1}y_{P1}$ broadband filters and photometric system are described in detail in Tonry et al. (2012).

PS1/MDS operated from late 2009 to early 2014. PS1/MDS consists of 10 fields (each with a single PS1 imager footprint) observed in $g_{P1}r_{P1}i_{P1}z_{P1}$ with a typical cadence of 3 d in each filter, to a typical nightly depth of ~ 23.3 mag (5σ); y_{P1} is used near full moon with a typical depth of ~ 21.7 mag. The standard reduction, astrometric solution, and stacking of the nightly images are done by the Pan-STARRS1 Image Processing Pipeline (IPP) system (Magnier 2006; Magnier et al. 2008) on a computer cluster at the Maui High Performance Computer Center. For the transients search, the nightly MDS stacks were transferred to the Harvard FAS Research Computing cluster, where they were processed through a frame subtraction analysis using the `photpipe` pipeline developed for the SuperMACHO and ESSENCE surveys (Rest et al. 2005; Garg et al. 2007; Miknaitis et al. 2007; Rest et al. 2014).

PS1-14bj was first detected in PS1/MDS imaging on 2013 November 22.6 (UT dates are used throughout this paper), at coordinates RA = $10^{\rm h}02^{\rm m}08.433^{\rm s}$, Dec = $+03°39'19.02''$ (J2000). The detection image was also the first image taken of this field after 2013 May 10.3, so we do not have any recent limits to constrain the explosion date further. The PS1/MDS light curve shows an unusually slow rise over an observed time scale of two months, and PS1-14bj was selected for follow-up spectroscopy. An initial MMT spectrum taken on 2014 March 8.3 proved inconclusive, so an additional spectrum was obtained with Gemini-North on 2014 March 28.4. The broad spectral features in those data show an excellent match with the earliest spectrum of the unusual H-poor SLSN SN 2007bi (Gal-Yam et al. 2009; Young et al. 2010), and an approximate redshift of $z \approx 0.54$ was determined by cross-correlating the SN spectrum with that of SN 2007bi. As the supernova faded, weak narrow-line [O III] λ5007 and Hβ emission from the host galaxy became visible, yielding a precise redshift of $z = 0.5215$, which is adopted throughout this paper. The somewhat higher redshift estimate obtained by comparison with SN 2007bi is due to the higher expansion velocity of that object compared to PS1-14bj (Section 4). We note that given this redshift, the observed peak magnitude of PS1-14bj is -20.75 mag (i-band). This is fainter than the proposed SLSN cutoff at -21 mag in Gal-Yam (2012), illustrating that such a cutoff is arbitrary.

We determine the time of peak light by fitting a low-order polynomial to our constructed bolometric light curve (Section 3.3), yielding a best-fit time of peak of MJD 56801.3 ± 5 days. All phases reported are relative to the time of peak light.

2.2. *Additional Photometry*

As PS1-14bj was discovered at the very end of PS1/MDS, we have continued to follow it up from other telescopes to continue the light curve. Addi-

tional optical imaging was mainly obtained with MMT-Cam[19], an f/5 imager on the 6.5 m MMT telescope; with the Low Dispersion Survey Spectrograph (LDSS3) and the Inamori-Magellan Advanced Camera for Surveys (IMACS; Dressler et al. 2006) on the 6.5 m Magellan telescopes; with the Gemini Multi-Object Spectrograph (GMOS; Hook et al. 2004) on the 8 m Gemini Telescopes as part of acquisition for spectroscopy; and some additional images from the Large Binocular Cameras on the 8.4 m Large Binocular Telescope (Speziali et al. 2008), the RETRactable Optical CAmera for Monitoring (RETROCAM; Morgan et al. 2005) on the MDM 2.4 m Hiltner telescope, and the 1.3 m McGraw-Hill telescope at MDM Observatory in direct imaging mode with the R4K detector. We also obtained two epochs of NIR imaging with the FourStar Infrared Camera on the 6.5 m Magellan/Baade telescope (Persson et al. 2008).

All optical images were bias-subtracted, flat-fielded and stacked using standard procedures in IRAF[20]. To correct for the underlying host galaxy flux, we used the ISIS subtraction package (Alard & Lupton 1998) to subtract off the PS1/MDS pre-explosion template images (Section 2.4) before measuring the SN flux in the subtracted images using aperture photometry.

The field of view and consequently the stars available for photometric calibration varies between the instruments we used to follow PS1-14bj. To ensure consistency, we first measured the light curve relative to two nearby stars that are present in all images. The absolute calibration was determined from a set of IMACS images, comparing photometry of > 10 stars in each filter to SDSS. All photometry has been corrected for foreground extinction according to Schlafly & Finkbeiner (2011) ($E(B-V) = 0.019$ mag), and is listed in Table 1. The light curves are plotted in Figure 2.

The FourStar images were calibrated, aligned and co-added using the IRAF/FSRED package (A. Monson 2013, private communication). As we lack pre-explosion host galaxy templates for subtraction in the NIR, we instead use the SED fit to the host galaxy photometry (Section 5) to estimate the expected host galaxy flux. We determine the total flux using aperture photometry, with the zero-point determined from 2MASS stars in the field, and subtract the expected host contribution numerically. The resulting J-band magnitudes are listed in Table 1. K_S-band imaging was also performed in the second epoch, but the detection is marginal and close to the expected host galaxy flux within the uncertainties. Image subtraction is needed to determine the SN contribution, and we therefore do not use the K_S-band data in further analysis.

2.3. *Spectroscopy*

We obtained 11 spectra of PS-14bj between 2014 March 8 and 2015 March 28 using the Blue Channel spectrograph on the MMT (Schmidt et al. 1989), IMACS and LDSS3C at Magellan, and both GMOS-N and GMOS-S on the 8 m Gemini telescopes. We use IRAF to per-
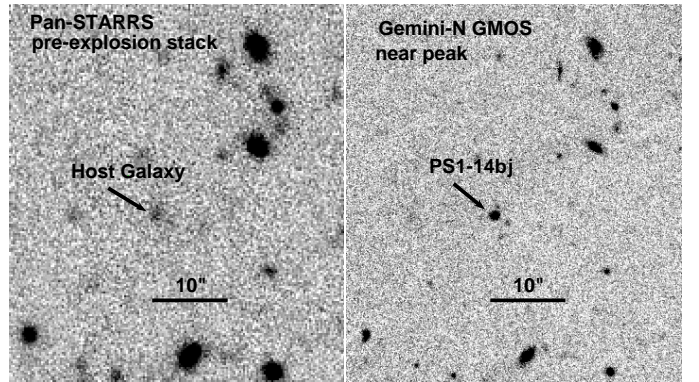
Figure 1. Stacked i_{P1} PS1/MDS pre-explosion image of the field around PS1-14bj (left), compared to an i-band image from GMOS taken near peak (right). A faint host galaxy is clearly seen at the supernova position. In the GMOS image, which has significantly better seeing ($0.4''$ FWHM, compared to $1.3''$ in the template), it appears that the host galaxy may have some structure or multiple components.

form bias subtraction, flat fielding, and spectral extraction. We use observations of spectrophotometric standard stars (archival in the case of GMOS) to apply a flux calibration and correct for telluric absorption. The final GMOS-N observation was taken in nod-and-shuffle mode (Glazebrook & Bland-Hawthorn 2001), but we find that the sky subtraction is adequate without performing the subtraction of nod pairs, so we simply shift and combine all exposures with the same grating tilt prior to spectral extraction. Observations taken in red-sensitive setups used order-blocking filters. The slits were generally aligned near the parallactic angle (Filippenko 1982), except at low airmass or with IMACS, which has an atmospheric dispersion compensator, so the relative flux scales should be reliable, as demonstrated below by comparison to the photometry in Section 3.2. In some cases, we combine spectra taken on consecutive nights or in setups with complementary wavelength coverage. A summary of all spectroscopic observations is given in Table 2 and the spectra are shown in Figure 3.

2.4. *Host Galaxy Photometry*

To search for a host galaxy, we stack the PS1/MDS data from the four observing seasons prior to the detection of PS1-14bj. No host is detected in the "standard" deep stacks (consisting of the 80 observations with best image quality), but by stacking all the available data (about 200 individual observations/filter) we are able to go significantly deeper at the expense of worse FWHM in the resulting stacks. A faint galaxy is detected at the position of PS1-14bj in all filters; as an example, the i_{P1} stack is shown in Figure 1. Photometry in a $2''$ aperture yields $g_{P1} = 24.57 \pm 0.15$ mag, $r_{P1} = 23.83 \pm 0.13$ mag, $i_{P1} = 23.93 \pm 0.15$ mag, and $z_{P1} = 23.51 \pm 0.16$ mag. We use these deep stacks as subtraction templates for the non-PS1 photometry (the PS1 photometry is already host subtracted as part of the pipeline). The properties of the host galaxy itself are discussed in Section 5.

2.5. *Comparison Data: LSQ14an*

LSQ14an is a supernova discovered by the La Silla Quest survey in early 2014, at coordinates RA = $12^h53^m47.83^s$, Dec = $-29°31'27.2''$. It was classified by PESSTO (Smartt et al. 2015) as a post-peak 2007bi-like
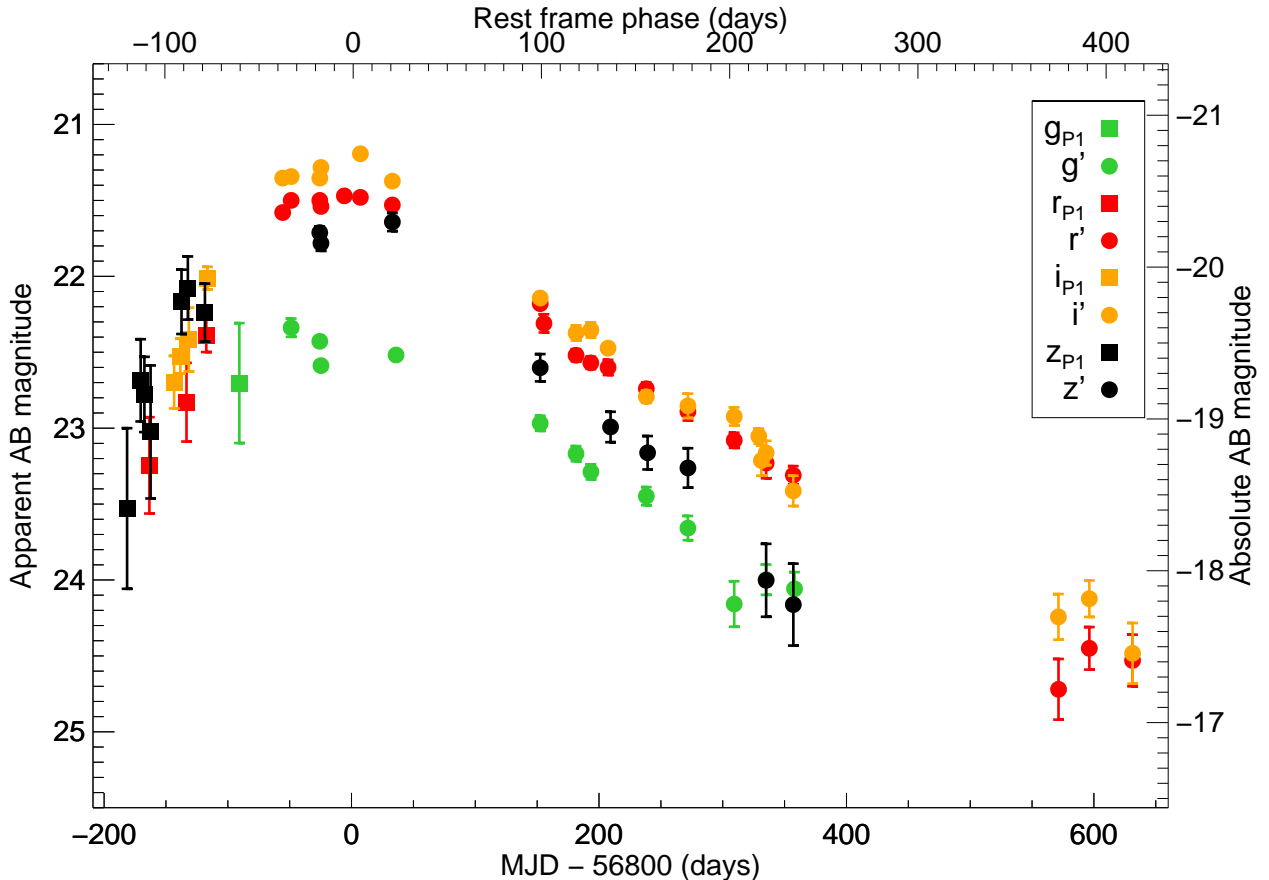
Figure 2. Observed light curve of PS1-14bj. The first 2.5 months of $r_{P1}i_{P1}z_{P1}$ data are from PS1/MDS, while the remaining photometry is from a variety of telescopes as detailed in Table 1. PS1-14bj was spectroscopically classified after PS1/MDS had ceased taking data and so there is a gap in coverage on the rise; there are also two gaps on the decline due to PS1-14bj being in solar conjunction. Note the long observed time scales.

SLSN at redshift $z = 0.163$ (Leget et al. 2014). We have obtained a spectroscopic sequence of LSQ14an, and find it to be a remarkably close match to PS1-14bj (Section 4). The details of our observations of LSQ14an are given in Table 3. In addition, $griz$ photometry was obtained with each spectrum; the g- and r-band light curves are shown in Figure 4. We lack supernova-free galaxy templates in our specific camera and filter combinations, and therefore the image subtraction method can not yet be applied to analyze the light curves in detail. However, our data demonstrates that LSQ14an was indeed discovered on the decline (as was inferred from the initial PESSTO spectrum), and furthermore that it is also a SLSN with a slow decline rate, establishing it as a reasonable comparison object for PS1-14bj. The host galaxy is visible in the Pan-STARRS 3π image stack, at $g_{P1} = 20.93 \pm 0.11$ and $r_{P1} = 20.50 \pm 0.12$ (Chen 2015; Inserra et al. in prep) indicating that the flattening of the lightcurve in Figure 4 is almost certainly due to contamination of the host.

The spectra of LSQ14an are used as a basis for comparison in Section 4. Full spectral analysis and further consideration of the light curve await proper host subtraction after the SN fades, which we defer to future work.

3. LIGHT CURVE AND ENERGETICS

3.1. *Light Curve Comparisons*

The r- and z-band light curves of PS1-14bj are shown in Figure 4, compared to other slowly-evolving H-poor SLSNe from the literature: SN 2007bi, PTF12dam, iPTF13ehe and PS1-11ap. We also show our own light curve of LSQ14an, establishing it as another slowly-evolving object. All light curves have been corrected for cosmological expansion following

$$M = m - 5\log(D_L/10 \text{ pc}) + 2.5\log(1 + z) \qquad (1)$$

(Hogg et al. 2002), where m is the apparent AB magnitude and D_L is the luminosity distance. This is not a full K-correction; filters have been chosen to correspond to approximately similar rest wavelengths as indicated in the legends in order to facilitate comparison. In both filters, the light curve of PS1-14bj is significantly broader than the other events, in particular having a significantly longer rise time than any of the other events, and a flatter light curve with a lower peak luminosity. In the bluer band, the decline of PS1-14bj appears shallower than the other events, but the decline in the redder filter is similar to the other events. The decay slope of LSQ14an appears to be even shallower than PS1-14bj, but the photometry
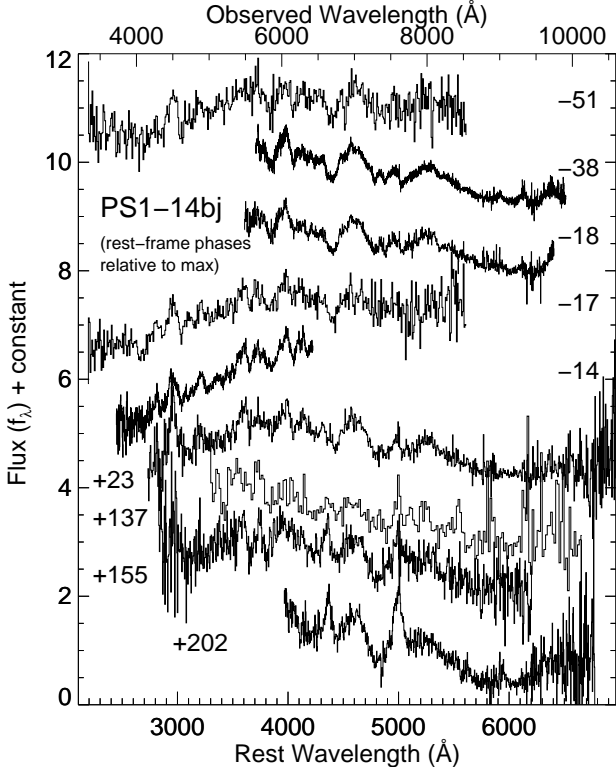
Figure 3. Spectroscopic sequence of PS1-14bj, labeled by the rest-frame phases relative to bolometric maximum light. The spectra have been binned for display purposes.

plotted for this event includes an unknown contribution from the host galaxy (Section 2.5).

Interestingly, the light curve decline is not entirely smooth particularly in i- and z-band (Figure 2), but shows some undulations around 100-200 days. The light curve of SN 2007bi shows a similar kink (Gal-Yam et al. 2009; Young et al. 2010), and recently Nicholl et al. (2016) showed that the well-studied SN 2015bn also displays a "knee" in the light curve decline. Such deviations from a smooth decline may therefore not be unusual in slowly-evolving SLSNe.

3.2. *Color Evolution and Blackbody Fits*

The observed color evolution of PS1-14bj is shown in Figure 5. The color evolution is almost flat over the > 300 days covered by our light curve data, and shows an overall trend towards *bluer* colors with time in $i - z$. This is different from the color evolution observed so far in virtually all H-poor SLSNe, which usually start out very blue but turn redder as the ejecta expand and cool (see e.g. PS1-11ap, shown in Fig. 5 for a more typical example). The near-constant color of PS1-14bj suggests there must be a sustained source of heating over very long timescales.

We fit blackbody curves to the SED of PS1-14bj in order to track the temperature and radius of the photosphere with time, using the IDL `mpfitfun`[21] framework to fit a Planck function to the observed photometry. Two example SEDs are shown in Figure 6, for the two epochs

where we also have NIR photometry. The spectra closest in time to the NIR photometry are also shown for comparison. The flux in g-band is affected by strong absorption, and including g-band in the fit leads to a cooler derived blackbody temperature and a larger blackbody radius.

Figure 7 shows the resulting blackbody temperatures (top) and radii (middle), showing fits both to all filters (black points) and excluding g-band (red points). The plotted error bars are the formal uncertainties returned from the blackbody fits given the photometry uncertainties. While the formal uncertainty is small (in many cases < 500 K and thus too small to be seen on the plot in Figure 7), the fact that the difference between the set of fits is larger than the calculated error bars indicates that the systematic uncertainty associated with line blanketing is the dominant source of uncertainty on the actual temperature. We note that the trends in temperature and radius are the same for both sets of fits, however.

The temperature fits show the same trends as are seen in the color evolution: the blackbody temperature is remarkably slowly evolving as well, and is in fact increasing with time over the entire time sampled by our light curve. With the overall flux declining, while the temperature is constant or increasing, the best-fit blackbody radius is decreasing as the light curve declines. We note that combining the estimated radius at peak (3–5×10^{15} cm) and photospheric velocity (5000 km s^{-1}; Section 4) yields a rise-time of 70–115 days, well within our observed rise.

3.3. *Bolometric Light Curve and Total Radiated Energy*

In order to construct a pseudo-bolometric light curve, we first sum up the observed photometry. In order to account for flux outside of our observed bandpasses, we add to this a blackbody tail redwards of the observed photometry, using the temperatures derived from our blackbody fits. For the purposes of this correction, we use the fits that exclude g-band. Blueward of the observed g-band, the spectra show that the flux is suppressed by line blanketing, and, in particular, not well approximated by a blackbody. We therefore do not attempt to add a correction for missing blue flux, and our reported bolometric light curve should be considered a lower limit. We do have a few spectra with coverage extending bluer than g-band; from summing the total flux in the 2014 April 28 Blue Channel spectrum bluewards of g-band, as well as approximating the spectral shape in the blue as a polynomial and extrapolating, we find that the missing flux is of order $\lesssim 5\%$ of the total.

The resulting bolometric light curve is shown in Figure 8, and the data is listed in Table 4. Open symbols show the light curve from only combining the observed flux at epochs where we have at least three filters, and the closed symbols include the bolometric correction to the red. For the earliest light curve points, where we lack color information, we assume the same SED shape as the earliest multi-filter epochs. Similarly, for the last three epochs we only have the $r - i$ color, and we estimate the bolometric luminosity by assuming the same bolometric correction as for the last two epochs with multi-color data. The $r - i$ color in our latest epochs is consistent with the previous epochs within the uncertainties, so this is not an unreasonable assumption. As the
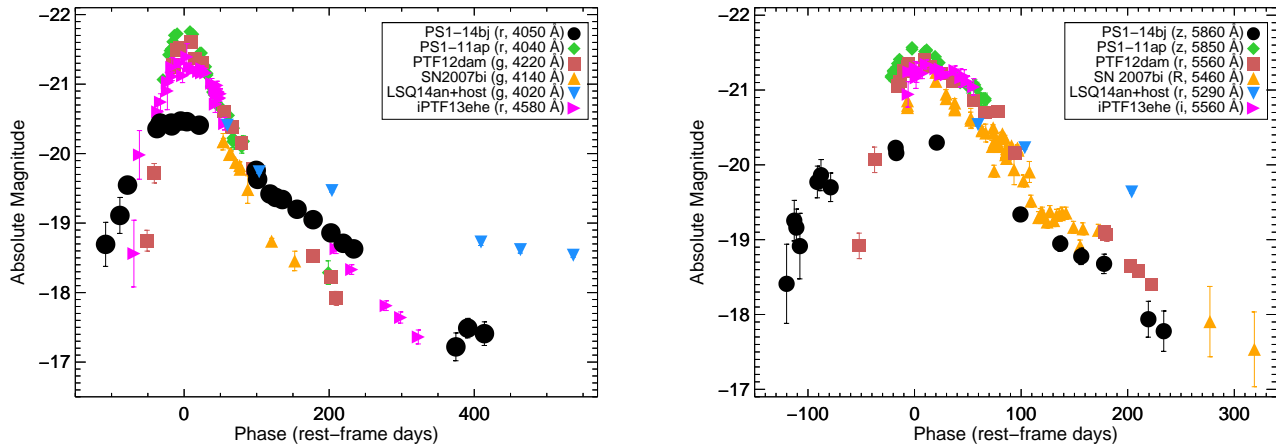
Figure 4. Light curve of PS1-14bj at effective wavelengths $4000\,\text{Å}$ (r-band, left) and $5800\,\text{Å}$ (z-band, right), compared to other "slowly-evolving" H-poor SLSNe: SN 2007bi (Gal-Yam et al. 2009; Young et al. 2010), PS1-11ap (Nicholl et al. 2013; McCrum et al. 2014), PTF12dam (Nicholl et al. 2013) and iPTF13ehe (Yan et al. 2015). PS1-14bj and PS1-11ap are both at redshift $z \sim 0.5$ while SN 2007bi and PTF12dam are at redshift $z \sim 0.1$; filters plotted are chosen to correspond to approximately the same rest wavelengths, and have been corrected for cosmological expansion. PS1-14bj shows a notably slower rise and flatter peak than PS1-11ap and PTF12dam, and a significantly shallower decline at a rest wavelength of $\sim 4000\,\text{Å}$ than the other objects. At a rest wavelength of $\sim 5800\,\text{Å}$, the decline rate of PS1-14bj is similar to the other slowly-evolving SLSNe, but still shows a significantly broader light curve and lower peak luminosity. The LSQ14an data have not had the host contribution subtracted due to the current lack of templates, but demonstrate that it is also has a slow decline rate.
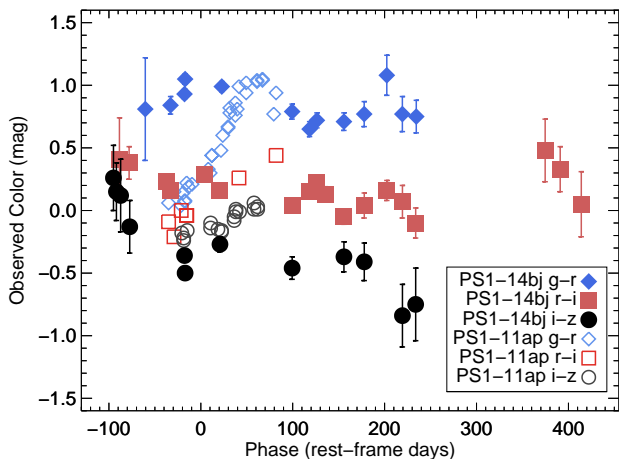

Figure 5. Color evolution of PS1-14bj (filled symbols). The open symbols show the more typical H-poor SLSN PS1-11ap (McCrum et al. 2014), which was at almost exactly the same redshift as PS1-14bj ($z = 0.524$), facilitating comparison. PS1-14bj is significantly redder than PS1-11ap in its early phases, particularly seen in the observed $g-r$ color. Also note the remarkably flat color evolution of PS1-14bj, with an overall trend towards bluer colors with time, particularly in $i - z$. In contrast, PS1-11ap (like most supernovae) turns redder with time.
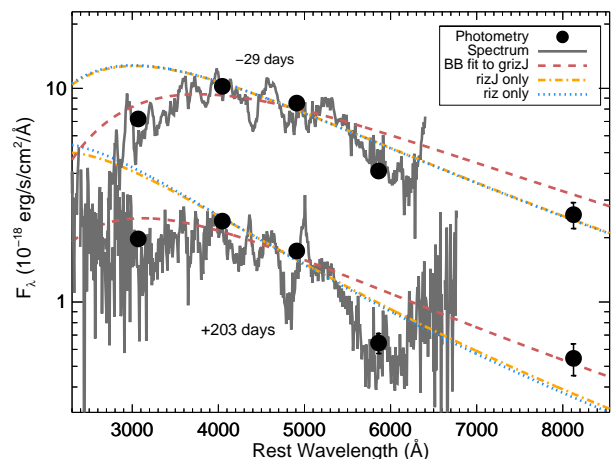

Figure 6. Example SED fits for the two epochs where we have J-band photometry. The black points show the photometry, while the spectra taken closest in time are shown in gray. The g-band flux is suppressed by line blanketing, and including it in the SED fit (red dashed curve) leads to a cooler inferred temperature and larger radius. We therefore exclude g-band measurements from our blackbody fits when calculating the bolometric correction in the red, and for most epochs only fit riz, here illustrated by the blue dotted curve. Including the J-band photometry (orange dot-dashed curve) yields a very similar fit, indicating that the riz fit is a reasonable approximation of the SED shape redwards of the observed bands.

color is somewhat different between these three epochs, we get different results depending on whether we scale from r- or i-band; we take the mean value as our best estimate. We caution, however, that at these late times the spectra are dominated by line emission rather than continuum, and so the blackbody assumptions used to derive the bolometric corrections will break down. The error bars of the latest light curve points are therefore likely underestimated.

The peak luminosity is 4.56×10^{43} erg s^{-1} or -20.45 mag. As can also be glanced from Figure 4, PS1-

14bj is significantly lower luminosity at peak than other slowly-evolving SLSNe. The early light curve decay (out to ~ 250 days) is well fit by exponential decay, with a best-fit slope of $(1.00 \pm 0.05) \times 10^{-2}$ mag day^{-1}. We note that this slope is very close to that of the decay of ^{56}Co to ^{56}Fe, which is 9.74×10^{-3} mag day^{-1}, and shown by the dashed gray line in Figure 7. However, while noisy, the latest light curve points (around 400 days) lie above
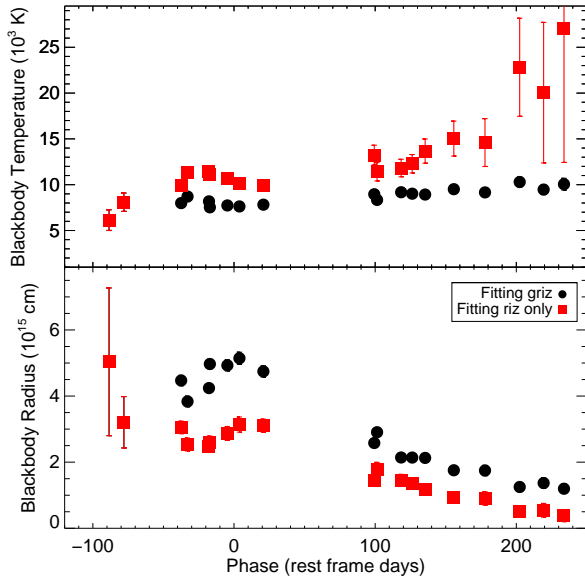
Figure 7. Blackbody temperature (top) and radius (bottom) of PS1-14bj. Black points show fits to all photometry, while the red points exclude *g*-band data (since the spectroscopy shows *g*-band is affected by line blanketing; Figure 6). The difference between the two sets of fits are generally larger than the derived error bars from the fit, suggesting that these line effects are the largest source of uncertainty in the absolute temperature. The general trends remain the same, however.
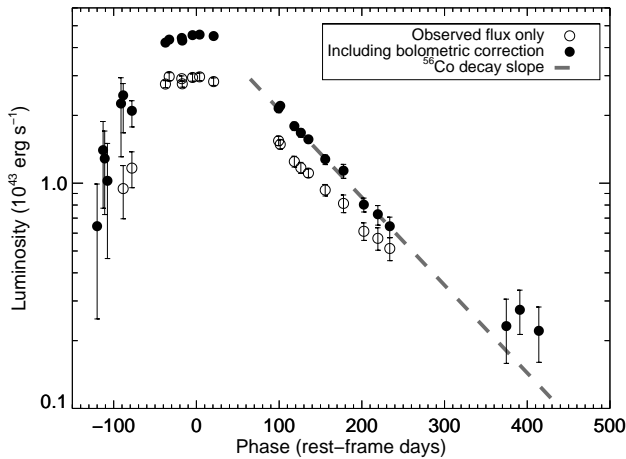

Figure 8. Bolometric light curve of PS1-14bj. The open symbols are created by summing all the flux at epochs where we have at least three filters, a strict lower limit. The filled symbols correspond to the bolometric light curve including a blackbody correction in the red. The decline luminosity is well fit by exponential decay, with a best-fit slope very close to that of pure Co decay, which is shown by the dashed gray line.

the ^{56}Co prediction; including these points give a best-fit decay slope of $(9.2 \pm 0.4) \times 10^{-3}$ mag day^{-1}.

We estimate the time of explosion from fitting a t^2 polynomial to the rise portion of the light curve, setting the explosion date at MJD 56607.0 (2013 November 11.0) ± 6.4 days, with most of the uncertainty being due to the noisy nature of the early light curve. This suggests
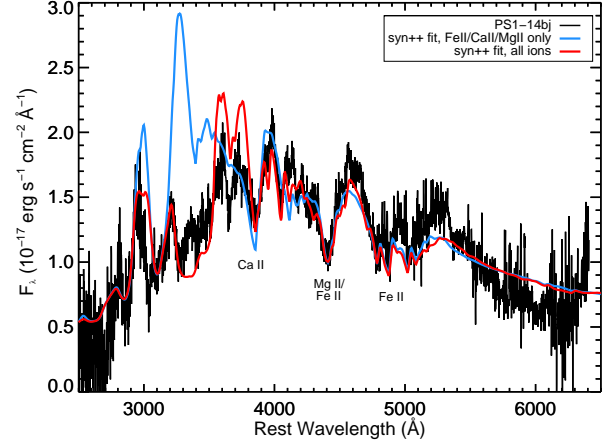

Figure 9. SYN++ fit to the near-peak spectrum of PS1-14bj. The main features are attributed to Ca II, Mg II and Fe II traveling at velocities 5000-9000 km s^{-1}, as shown in the blue-line fit that only contains these ions. The full fit also includes Co II, Ni II and Ti II, which significantly improves the fit in the blue.

that PS1-14bj exploded a short time before PS1/MDS resumed observing the field on 2013 November 22.6, so our observed data covers most of the rise. We note that a t^2 polynomial is an excellent fit to the rise of the light curve, with a reduced χ^2 value of 1.01. We therefore do not find any evidence for a double-peaked light curve, as was seen in LSQ14bdq (Nicholl et al. 2015), and argued to possibly be a ubiquitous feature of H-poor SLSNe (Nicholl & Smartt 2016). Similarly, we estimate the time of peak by fitting a forth-order polynomial to the data near peak, and find the best-fit time of peak to be MJD 56801.3 ± 5 days; here the uncertainty is mainly due to the flatness of the peak. This gives a rise time estimate of 128 days in the rest frame, the longest observed in a SLSN so far.

Integrating our bolometric light curve over time gives an estimate of the total radiated energy: $E_{\rm rad} \simeq 7.6 \times 10^{50}$ erg. This number is comparable to other SLSNe; the lower peak luminosity is compensated by the broad light curve.

4. SPECTROSCOPIC EVOLUTION

To identify the features and estimate the velocities in the photospheric spectra, we use the spectral synthesis code SYN++ (Thomas et al. 2011). Figure 9 shows the fit to the combined day -17/day -14 spectrum, with the main features marked. The gray line is a fit including only Fe II, Mg II and Ca II, which reproduces the main absorption features well. The absorption feature near 3840 Å is well fit by Ca II, and the narrow absorptions between 4500–5300 Å are reasonably fit by Fe II. The feature near 4390 Å is usually attributed to Mg II (e.g., Gal-Yam et al. 2009), although we find it is best fit by a blend of Mg II and Fe II. Including Co II, Ni II and Ti II (red line) helps suppress the flux in the blue, and improves the overall fit. Velocities used in the fit range from 5000–9000 km s^{-1}, with Fe II "detached" to match the narrow absorption features. We do not find any significant velocity evolution fitting the spectra from day -38 to day $+23$.

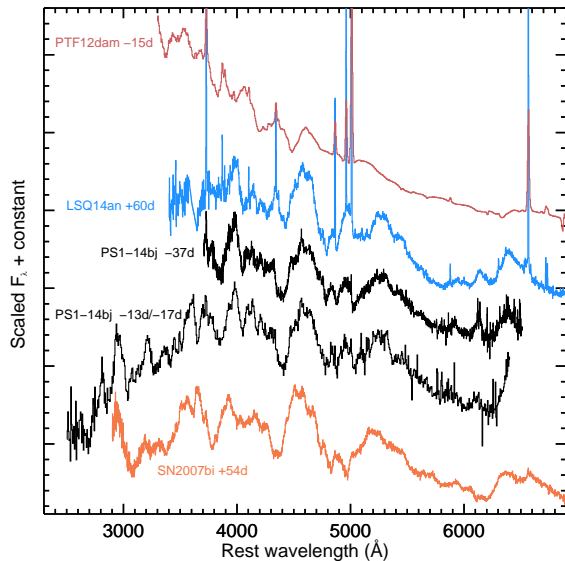Figure 10 shows a comparison of the early-time spec-

Figure 10. Early-time spectra of PS1-14bj compared to other slowly-evolving SLSNe (Nicholl et al. 2013; Gal-Yam et al. 2009). The spectra are dominated by features from Ca II, Fe II and Mg II, similar to the earliest available spectra of SN 2007bi. The early-time spectrum of PTF12dam, in contrast, is dominated by O II features and is much bluer than PS1-14bj at the corresponding phase.
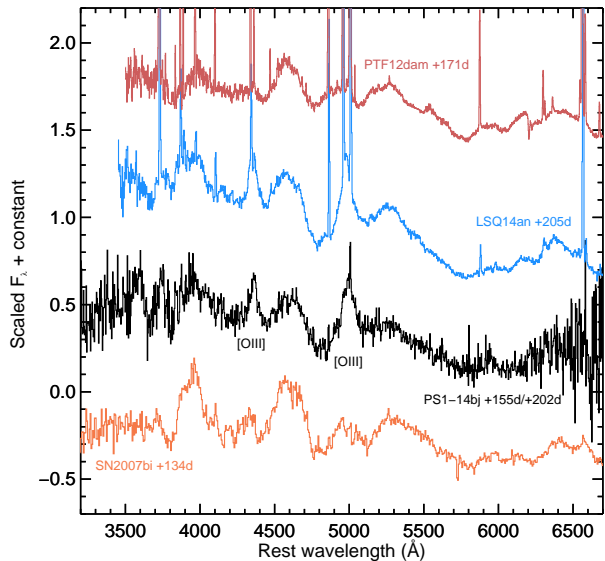

Figure 11. Late-time spectrum of PS1-14bj compared to other slowly-evolving SLSNe (Nicholl et al. 2013; Young et al. 2010). Spectra are labeled with their rest-frame phases relative to maximum light. Notably, PS1-14bj and LSQ14an both show strong emission features near 4360 Å and 5000 Å that are not seen in the other SNe, and which we identify as [O III] emission. Note that these spectra are not host-subtracted, so there is a contribution from the host galaxy to the continuum in the spectra as displayed. The host-subtracted photometry of PS1-14bj shows that its color temperature stays nearly constant around 8000-10,000 K to very late times, however, so not all of the blue continuum can be attributed to the host.

tra of PS1-14bj to three other slowly-evolving H-poor SLSNe: SN 2007bi, LSQ14an and PTF12dam. There are no pre-peak spectra available for SN 2007bi, but the earliest spectrum (at phase +54 days) is remarkably similar to the PS1-14bj spectra, with the main difference being that SN 2007bi has slightly higher photospheric velocities of 12,000 km s^{-1} (Gal-Yam et al. 2009). LSQ14an at +60 days is also very similar to PS1-14bj despite the difference in phase, including the low velocities. This speaks to the very slow spectroscopic evolution of these objects, mirroring the slow light curves. PTF12dam, in contrast, shows a much bluer spectrum with O II features pre-peak, similar to more typical H-poor SLSNe (Quimby et al. 2011), consistent with its much higher temperatures near peak.

Late-time spectra are shown in Figure 11, where we have combined the +155 and +202 days spectra of PS1-14bj for better S/N and wavelength coverage. The spectrum shows a mix of absorption and emission features, and in particular has not turned fully nebular despite the late phase. Such slow evolution is similar to what was seen in SN 2007bi, which did not turn fully nebular until > 400 days past peak. The four SNe shown in Figure 11 show many similarities in their late-time spectra, but with one prominent difference: PS1-14bj and LSQ14an both show strong emission features around 5000 Å and 4360 Å. These features are not present in SN 2007bi or PTF12dam, and indeed have not been previously seen in SLSN spectra. We tentatively identify these features with [O III] λ4363 and $\lambda\lambda$4959,5007.

A zoom-in of these features is shown in Figure 12; the FWHM of the line at 4360 Å is about 3400 km s^{-1}. The feature around 5000 Å is broader with a slightly asymmetric profile — if this is indeed [O III] emission this can

be understood as the blended emission from the stronger line at 5007 Å and the line at 4959 Å. The righthand panel of Figure 12 shows a double-Gaussian fit to the emission near 5000 Å, with the line ratios and central wavelengths fixed to those expected for $\lambda\lambda$4959,5007 and with the same FWHM as for the λ4363 line. This provides a reasonable match to the line profile, although there is excess blue flux compared to the fit particularly in the line at 5007 Å.

Broad [O III] emission is usually not seen in SNe until years to decades following core-collapse, as well as in O-rich supernova remnants (e.g., Milisavljevic et al. 2012). Instead, the dominant emission from oxygen tends to be [O I] $\lambda\lambda$6300,6364, which indeed is what was eventually seen in SN 2007bi and PTF12dam (Gal-Yam et al. 2009; Young et al. 2010; Nicholl et al. 2013; Chen et al. 2015). We discuss possible sources of the ionizing flux in Section 6. We note that the low flux ratio of [O III] $\lambda\lambda$4959,5007 to [O III] λ4363 ($\lesssim$ 3) implies that the electron density in the [O III]-emitting region is near the critical density for these transitions ($\gtrsim 10^6$ cm^{-3}; e.g. Fesen et al. 1999). A similar [O III] line ratio was observed in the Type IIn SN 1995N, with a derived density in the [O III] emitting region of 3×10^8 cm^{-3} (Fransson et al. 2002).

5. PS1-14BJ HOST GALAXY

The host galaxy of PS1-14bj is detected in our deep PS1/MDS pre-explosion stacks (Section 2.4; Figure 1) in filters $g_{P1}r_{P1}i_{P1}z_{P1}$. r_{P1} corresponds approximately
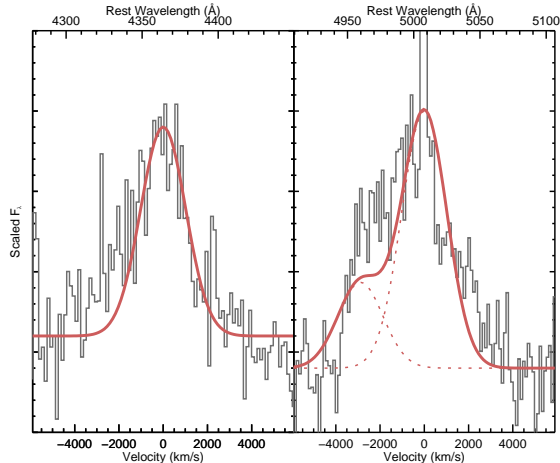
Figure 12. Zoom-in on the line profiles of the emission features at 4360 Å and 5000 Å in the late-time spectrum of PS1-14bj. The red line shows a Gaussian fit with a FWHM of 3400 km s^{-1}, assuming the correct identifications for these features are [O III] λ4363 and [O III] λλ5007,4959.

to rest-frame B-band, giving an absolute magnitude $M_B \simeq -18.1$ mag. Fitting a galaxy model to the SED using the FAST code (Kriek et al. 2009), we find a best-fit galaxy mass of $\log(M_{gal}/M_\odot) = 8.5 \pm 0.5$. Other galaxy properties going into the model grid (such as extinction, stellar population age and star formation rate) are not well constrained by our relatively noisy galaxy photometry. The detection of narrow [O III] λ5007 and Hβ emission from the host galaxy in our late time spectra indicates that the host galaxy is star forming. While we do not detect narrow Hα, we can calculate a lower limit on the star formation rate from the Hβ flux assuming no host galaxy extinction. Using Hβ and the relation from Kennicutt (1998) we calculate a star formation rate of $\gtrsim 0.2\ M_\odot$ yr^{-1}.

In the context of H-poor SLSNe, the host galaxy of PS1-14bj is quite typical, with both its absolute magnitude and mass close to the median values found in the compilation of Lunnan et al. (2014) ($\langle M_B \rangle = -17.6$ mag and $\langle M_{gal} \rangle = 2 \times 10^8 M_\odot$, respectively). While there are relatively few slowly-evolving H-poor SLSNe known, their host galaxies so far do not appear to be different from the bulk of H-poor SLSNe, spanning a similar range of properties (Chen et al. 2015); PS1-14bj continues this trend.

6. ENERGY SOURCES

In this section, we discuss potential energy sources for PS1-14bj, and compare the observed properties to model predictions.

6.1. *Radioactive Decay: PS1-14bj as a PISN*

^{56}Ni decay is usually ruled out as the power source of ordinary H-poor SLSNe from the shapes of their light curves, with the combination of high peak luminosities and relatively fast-evolving light curves leading to an unphysical solution with $M_{Ni} \gtrsim M_{ej}$ (e.g., Chomiuk et al. 2011; Lunnan et al. 2013). Given the broad light curve and lower peak luminosity of PS1-14bj, combined with the decline rate matching the decay of ^{56}Co, we explore radioactive decay.

Figure 13 shows ^{56}Ni-powered fits to the bolometric light curve of PS1-14bj, following Arnett (1982) and Valenti et al. (2008). This is essentially a scaled-up model of a Type Ic supernova, with the shape of the light curve determined from two main parameters: the total Ni mass, M_{Ni}, and the diffusion time through the ejecta $\tau_m \propto \kappa^{1/2} M_{ej}^{3/4} E_K^{-1/4}$, where κ is the opacity, M_{ej} the total ejecta mass, and E_K the kinetic energy. Using the velocity at peak measured from our spectra, $\simeq 5,000$ kms^{-1} and an opacity $\kappa = 0.1$ cm^{2}g^{-1}, we derive a total ^{56}Ni mass $M_{Ni} \sim 10$ M$_\odot$ and a total ejecta mass $M_{ej} \sim 52$ M$_\odot$ for the best-fit model, which has a reduced χ^2 value of 1.9. Note that the derived mass here scales inversely with the assumed opacity, which is uncertain by at least a factor of two in either direction (see Appendix D of Inserra et al. 2013 for a discussion). As a result, the inferred ejecta masses are also uncertain by at least a factor of two. This caveat applies to any mass estimates also in the following sections. The Ni-powered model is a good fit to the data through ~ 200 days past peak, but underpredicts the data points measured at ~ 400 days, suggesting that even if ^{56}Ni decay powers the main peak a different mechanism is likely dominating at these late times. We caution, however, that the bolometric correction of these last three points is uncertain, so the departure from the ^{56}Co decay slope may not be significant. The kinetic energy of this model is 2.2×10^{52} erg, (subject to the same caveats regarding effective opacity, and thus also uncertain by at least a factor of two; see also Wheeler et al. 2015). This gives a ratio of radiated to kinetic energy is $\sim 3\%$, of the same order as is seen in Type Ibc SNe.

If ^{56}Ni is the power source, the inferred nickel mass and total ejecta mass imply that PS1-14bj likely exploded as a pair-instability SN rather than a core-collapse SN. Figure 14 shows the light curve of PS1-14bj compared to the theoretical PISN light curves from Kasen et al. (2011), Dessart et al. (2013) and Kozyreva et al. (2014). Overall, PS1-14bj is a reasonable match to the shape of these light curves, with a luminosity intermediate between the He100 and He110 models. It does have a flatter light curve peak and lower peak luminosity than the similar-width PISN light curves, however. Unlike the simple Arnett model fit in Figure 13, these light curves are derived from radiation hydrodynamics modeling of the supernova explosions given several different progenitor models, and therefore do not have the freedom to tune the nickel and ejecta mass separately as in the simple Arnett fit. This explains why the fit in Figure 13 can better reproduce the flatter light curve shape, even though both the PISN models and the Arnett model are essentially Ni-powered. The PISN models have the same problem as the Arnett model in that the light curve points around ~ 400 days lie above the model prediction. We note that while not a perfect match to the theoretical expectation, PS1-14bj at least shows that there exist SLSNe with the broad light curves and long rise times expected by PISN models.

Moriya et al. (2010) presented core-collapse models for the light curve of SN 2007bi, showing that it could also be reasonably fit as an extreme core-collapse event rather than a PISN. In their model, the light curve is fit by the explosion of a 43 M$_\odot$ carbon-oxygen core, producing 6 M$_\odot$ of ^{56}Ni, and thus demonstrating that such large

Ni masses need not be the result of a PISN. The main discriminant between the core-collapse and PISN models is the supernova rise time, with the core-collapse having a lower ejected mass and thus a shorter rise time. PS1-14bj is not a good match to their core-collapse model, however: its rise time of $\gtrsim 125$ days, as well as the relatively low velocities on the rise, are better matched by their PISN model. Thus, if PS1-14bj is powered by ^{56}Ni it is more consistent with a PISN than an extreme core-collapse SN interpretation.

Arguing against a PISN/^{56}Ni model of PS1-14bj, however, are the color and spectroscopic evolution. While PS1-14bj is redder than a typical SLSN on the rise, it is still bluer than the expected colors of a PISN explosion due to the large amount of line blanketing from ^{56}Ni (e.g., the models of Dessart et al. 2012, 2013 have a maximum photospheric temperature of ~ 6000 K). The discrepancy grows worse after peak, as PISN models (or indeed any ^{56}Ni-powered model) predict the color turning redder on the light curve decline, whereas PS1-14bj shows a nearly constant color that, if anything, turns bluer. We note that the 250M model of Kozyreva et al. (2014) shows a temperature plateau for about 200 days up to and around peak light, but even this model cools to a color temperature of ~ 5000 K on the decline.

The spectral evolution of PS1-14bj also does not match what is expected from a PISN model. Kasen et al. (2011) found a reasonable match between the spectra of their He100 model at 100 days after explosion with the earliest available spectra of SN 2007bi, despite not explicitly tuning the model. Given the similarity between the two objects, that model should also be a reasonable match to the spectra of PS1-14bj near maximum light, except for the difference in expansion velocities. However, the spectra of the He100 model show significant evolution over time, with a smooth and relatively blue spectrum at 50 days after explosion evolving to a very red and line-blanketed one at 250 days (their Figure 9; Kasen et al. 2011). The spectra of PS1-14bj do not show such a rapid evolution and the models would not be a good match to our earliest and latest spectra (Figure 3). Recently, Jerkstrand et al. (2016) calculated model nebular phase spectra of PISNe, which are also not a good match to our late-time spectra. Specifically, their models have very little flux emerging bluewards of 5000 Å and are dominated by lines from Fe II in the wavelength range covered by our spectra. Some contributing flux from [O I] $\lambda\lambda 6300,6364$ is seen in their models, but no higher-ionization species of oxygen are predicted. Beyond the theoretical models, the fact that [O III] is not seen in nebular spectra of ordinary core-collapse SNe is in itself an argument against ^{56}Ni decay being the sole power source.

6.2. Magnetar Models

Since radioactive decay cannot be the energy source for the majority of SLSNe, several alternatives have been proposed. One possible energy source is the rotational energy of a newborn neutron star rapidly spinning down in a strong magnetic field. Theoretical calculations show that in the regime with initial spin of a few milliseconds and magnetic field of $10^{14} - 10^{15}$ G, the magnetar spin-down time is comparable to the diffusion time through the supernova ejecta, producing a long-lived en-
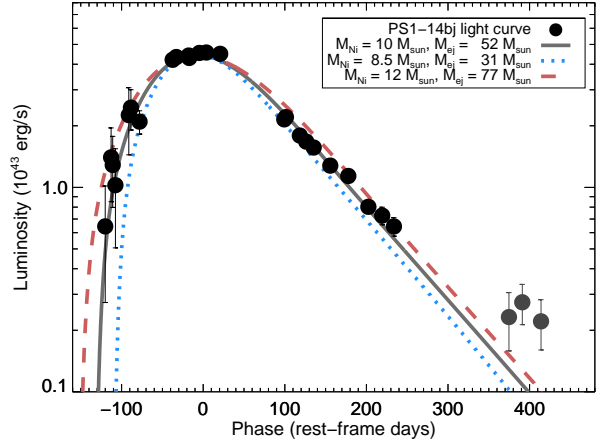

Figure 13. Fits to the light curve of PS1-14bj, using a Ni-powered model following Arnett (1982). The observed bolometric light curve can be reproduced with a model having a total ^{56}Ni mass of 10 $M_\odot$, and a total ejecta mass of ~ 50 $M_\odot$. Note that the bolometric correction of the last three points (colored gray) is highly uncertain, so the departure from the ^{56}Co decay slope may not be real.
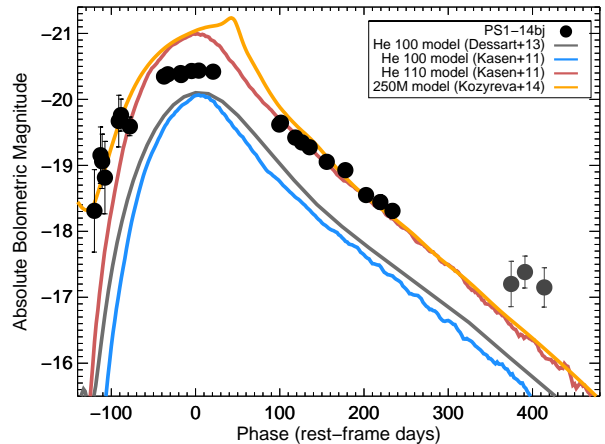

Figure 14. PS1-14bj bolometric light curve (black points) compared to theoretical PISN light curves from Kasen et al. (2011), Dessart et al. (2013) and Kozyreva et al. (2014). PS1-14bj has a lower peak luminosity compared to its width than the theoretical curves, but matches the overall long timescales well.

ergy injection that can significantly boost the optical radiation (Kasen & Bildsten 2010; Woosley 2010). Magnetar models have successfully been able to reproduce the light curves and other basic observed properties of a range of SLSNe (e.g., Chomiuk et al. 2011; Inserra et al. 2013; Lunnan et al. 2013), including those with slow decay time scales such as SN 2007bi (Dessart et al. 2012; Nicholl et al. 2013).

The key parameters of the magnetar model are the initial spin period P, which sets the total amount of rotational energy as $E_p \simeq 2 \times 10^{52}$ erg $\times (P/1 \text{ ms})^{-2}$; the magnetic field, which together with the initial period sets the spin-down timescale as $\tau_p \simeq 4.7$ days $\times (P/1 \text{ ms})^2 \times (B/10^{14} \text{ G})^{-2}$, and the total ejecta mass which sets the diffusion timescale τ_m as before. The resulting luminosity can then be solved for semi-analytically as

$$L(t) = \frac{2E_p}{\tau_p \tau_m} e^{-(\frac{t}{\tau_m})^2} \times \int_0^t \frac{1}{(1 + t'/\tau_p)^2} e^{(\frac{t'}{\tau_m})^2} \frac{t'}{\tau_m} dt'. \quad (2)$$

This suggests that in order to create a magnetar-powered SLSN with slow timescales, we need some combination of a larger ejecta mass (increasing the diffusion time) and larger ratio of P/B (increasing the spin-down timescale) compared to more typical SLSNe. Since P sets the total energy scale, which is not that different in PS1-14bj to other SLSNe, in practice this means we require a weaker magnetic field.

The green-dotted curve in Figure 15 shows the best-fit three-parameter magnetar model to the light curve of PS1-14bj. This model has an initial spin of 3.1 ms, a magnetic field of 10^{14} G, and a total ejecta mass of 22.5 $M_\odot$. It does a decent job of reproducing the overall broad light curve, but overpredicts the flux at late times and also starts declining earlier than the observed light curve; the reduced χ^2 of the fit is 2.9.

Overpredicting the flux on the late light curve decline is a common problem of magnetar models, but can be overcome if the assumption that all of the spin-down energy from the magnetar is being thermalized in the ejecta is relaxed. As the ejecta expand, they become optically thin to hard emission and significant amounts of γ- and X-ray photons can escape. Wang et al. (2015) considered this effect for SLSNe, and parametrized the changing opacity to γ-rays as $\tau_\gamma = At^{-2}$, so that Equation 2 is modified by the expression $(1 - e^{-At^{-2}})$ (Chatzopoulos et al. 2009, 2012). Including this term, the purple-dashed curve in Figure 15 shows the best fit to PS1-14bj, found by first finding the best three-parameter fit to the data on the rise through peak, and then adjusting the leakage parameter to fit the decline. The model shown also has an initial spin of 3.1 ms but a lower magnetic field of 5×10^{13} G, a slightly lower ejecta mass of 16 $M_\odot$, a leakage parameter $A = 5.5 \times 10^{14}$ s^2 and a reduced χ^2 value of 1.9. This value of A is within the range of typical values for CCSNe ($10^{13} - 10^{15}$ s^2) though lower by a factor of ~ 5 than what one would derive from Equation 4 of Wang et al. (2015) using the mass derived in the magnetar model and the velocities we measure from the spectra ($A \propto \kappa_\gamma M_{\rm ej}/v^2$), suggesting either a lower effective gamma-ray opacity κ_γ, or that the assumptions of uniform ejecta density distribution and constant expansion velocity may not apply.

While the overall shape of the light curve can be fit by a magnetar model, this class of models also meets a problem in explaining the observed color evolution, particularly at late times. Modeling the temperature evolution on the rise generally requires hydrodynamical simulations outside of the scope of this paper, but on the decline the magnetar model predicts that the ejecta is swept into a shell moving at constant velocity, and we can estimate the temperature by assuming blackbody radiation and a radius expanding linearly with time at the predicted velocity. For either version of the magnetar model this leads to a blackbody temperature decreasing with time, which is not what we observe for PS1-14bj (Figure 7).

Again, this simple calculation does not account for radiation from the magnetar itself escaping, however; one
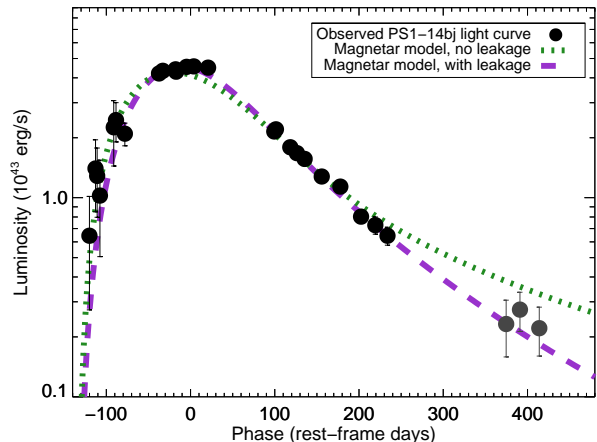

Figure 15. Magnetar model fits to the light curve of PS1-14bj. The green dotted curve is the best fit basic magnetar model, while the purple dashed curve is the best-fit model when allowing for late-time hard emission leakage. Without including the leakage term, the luminosity on the decline is overpredicted.

could imagine a scenario where the late-time heating seen in PS1-14bj is due to such X-ray to UV breakout from the central power source. Similarly, the [O III] lines could arise from O-rich ejecta being ionized from within becoming visible; we note that ionization calculations of a pulsar wind nebula inside expanding SN ejecta predict [O III] $\lambda 5007$ to be the strongest line in the optical window in the H- and He-free case (Chevalier & Fransson 1992). Although these calculations were done considering the scenario of a much weaker pulsar wind nebula than the magnetar considered here, and considered the line emission at somewhat later times than our observations, it demonstrates that such a late-time optical signature of the central engine is at least plausible.

6.3. CSM Interaction

Interaction between the SN ejecta and H-free CSM is a third alternative for powering SLSNe (Chevalier & Irwin 2011; Ginzburg & Balberg 2012; Moriya & Maeda 2012; Moriya et al. 2013; Chatzopoulos et al. 2012), and has been shown to reproduce the light curves of a wide range of SLSNe, including H-poor ones with slow evolution such as PTF12dam and SN 2007bi (Chatzopoulos et al. 2013; Nicholl et al. 2014; Chen et al. 2015). Light curves from CSM interaction depend on a number of parameters describing the mass, extent and profile of the CSM, and generally requires hydrodynamical modeling outside of the scope of this paper. For an order-of-magnitude estimate of the required CSM mass, we consider the simplified case of shock breakout from a dense wind described in Chevalier & Irwin (2011). Here, the CSM profile is described as a wind with $\rho_{\rm CSM} = Dr^{-2}$ ($= 5 \times 10^{16} D_* r^{-2}$ in cgs units) out to some radius R_w, where D_* is a constant. The diffusion time t_d scales with this density parameter as $t_d = 19.4 \kappa D_*$ (days), where κ again is the opacity. Taking the observed rise time (~ 128 days) as an estimate of t_d, for an opacity $\kappa = 0.1$ cm^2 g^{-1} as in the other models, we get a density parameter $D_* \simeq 66$. The wind radius R_w is approximately the blackbody radius at peak ($\sim 2.5 \times 10^{15}$ cm); integrating the density profile we get a required wind mass of $\simeq 50$ $M_\odot$. Again,

the derived mass scales inversely with the assumed opacity; if we instead use $\kappa = 0.2$ cm^2 g^{-1} (appropriate for a fully ionized metal-dominated gas), the derived mass goes down by a factor of two.

This number is subject to a lot of simplifying assumptions, but serves to illustrate that powering a light curve as luminous and as slow as PS1-14bj's with CSM interaction will require a CSM mass of tens of solar masses. Alternatively, the unusually long risetime of PS1-14bj might also be accommodated by invoking an unusual CSM density profile, as was necessary to explain the Type IIn SN 2008iy, which had the longest measured risetime of a supernova known to date (> 400 d; Miller et al. 2010).

Currently available CSM interaction models (e.g., Dessart et al. 2015) do not produce spectra that have the broad P-Cygni features exhibited by PS1-14bj on the rise and near maximum light (Figure 10). Instead, the computed spectra tend to exhibit strong emission lines on a continuum with only narrow P-Cygni features blueshifted by the wind velocity. However, only the hydrogen-rich case of SLSN-II, analogous to normal SNe IIn, has been explored in any detail. We do have spectra both at peak (+22 days) and at late times (+202 days) that go sufficiently red to cover Hα, and we do not detect Hα emission at either epoch — this indicates that the CSM material around PS1-14bj would have to be H-poor.

Rather than being the primary power source for the light curve, CSM interaction could also come into play at later times as the expanding SN ejecta encounter a previously ejected shell of material. Evidence for delayed interaction with a CSM shell was recently seen in the SLSN iPTF13ehe (Yan et al. 2015), which was originally classified as a SN 2007bi-like slowly-evolving SLSN, but developed broad Hα emission in its late-time spectra. This emission was interpreted to originate from interaction between the ejecta and a H-rich shell located at a radius $\sim 4 \times 10^{16}$ cm, and from the PTF sample of SLSNe with late-time spectra they estimate that such interaction may be present in at least 10-15% of "H-poor" SLSNe. In the Type Ic SN 2010mb, Ben-Ami et al. (2014) argued that interaction with ~ 3 M$_\odot$ of O-rich material was responsible for the slowly-declining light curve, blue continuum and strong [O I] λ5577 emission seen at late times.

Similarly, CSM interaction could be the source of the persistent blue continuum and [O III] lines seen in PS1-14bj. In particular, broad [O III] emission has been seen in several core-collapse SNe with interaction in years to decades after explosion and in SN remnants (Fesen et al. 1999; Milisavljevic & Fesen 2008), and interpreted as O-rich ejecta being ionized by the reverse shock. A similar feature was recently seen in the Type Ib SN 2014C at a phase of +282 days past maximum light, also accompanied by Hα, X-ray and radio emission all consistent with CSM interaction (Milisavljevic et al. 2015; Margutti et al. 2016). We note that the line widths of 3000-4000 km s^{-1} seen in PS1-14bj suggest that the [O III] emission is originating in the ejecta rather than in shocked CSM, likely arising in the freely expanding ejecta being illuminated by the X-rays from the reverse shock (Fransson 1984; Chevalier & Fransson 1994). Alternatively, if the [O III] lines are instead originating in

an oxygen-dominated CSM shell, this shell would have to be moving at higher velocities than are typically seen in CSM interaction in order to explain the line widths.

In the scenario where CSM interaction is responsible for the late-time heating of PS1-14bj, iPTF13ehe (Yan et al. 2015) makes for an interesting comparison. In particular, while the broad Hα feature in iPTF13ehe was interpreted as a result of interaction, iPTF13ehe did not show any corresponding [O III] features like we see in PS1-14bj. At face value this indicates that the temperature and density conditions in the oxygen-emitting region would be different between the two objects. We note, however, that in other SNe with interaction signatures and late-time [O III] emission, the [O III] features are much weaker than Hα (Fesen et al. 1999; Milisavljevic et al. 2015). If the flux ratio of Hα to [O III] was similar in iPTF13ehe to these previous objects, we would not expect to see it above the noise level even if present. Therefore, while we cannot say much quantitatively about the ionization conditions in iPTF13ehe versus PS1-14bj, they both illustrate the importance of late-time spectra in shedding light on the nature of SLSN-I.

If we assume that the [O III] lines in PS1-14bj are arising as a result of CSM interaction, we can estimate the distance to the shell based on the time at which the features emerge and the velocities of the SN ejecta. The minimum value for the forward shock velocity is the maximum velocity in our fit to the spectrum ($\simeq 10,000$ km s^{-1}), and the broad [O III] line is detected in our +137 day spectrum, corresponding to ~ 265 days after our estimated explosion date. This yields a shell distance of $\sim 2 \times 10^{16}$ cm, similar to what was derived for iPTF13ehe (Yan et al. 2015).

7. CONCLUSIONS

We have shown that PS1-14bj is an unusually slowly evolving SLSN with a number of peculiar properties. Its key observed features can be summarized as follows:

- An exceptionally slow rise to maximum light, observed to be $\gtrsim 125$ days, the longest yet reported in the literature for a H-poor SLSN. Independent of model, this implies a large ejecta mass.

- Continued slow evolution, with a nearly-flat peak and exponential decline over the first ~ 250 days past peak at a best-fit rate of $(1.00 \pm 0.05) \times 10^{-2}$ mag day^{-1}, a remarkably close match to fully-trapped ^{56}Co decay.

- A peak bolometric luminosity of 4.6×10^{43} erg/s, and an estimated total radiated energy of $\gtrsim 7.6 \times 10^{50}$ erg.

- Unusual color evolution, with the color temperature rising prior to peak, and staying constant within our uncertainties around 8,000-10,000 K through the peak and decline.

- A spectrum near peak dominated by features of Mg II, Ca II and Fe II, similar to other slowly-evolving SLSNe including SN 2007bi, although with lower velocities.

- A late-time spectrum (150-200 days past peak) with strong emission features which we identify as [O III] $\lambda 4363$ and [O III] $\lambda\lambda 4959,5007$, with a velocity width of 3000-4000 km s^{-1}.

All of these properties taken together are not easily explained by any of the single models suggested to power SLSNe. The long rise time, initially red colors, and decline rate initially following ^{56}Co decay would support a PISN interpretation. In the classification scheme of Gal-Yam (2012), PS1-14bj is similar to other objects identified as SLSN-R, such as the prototype SN 2007bi (Gal-Yam et al. 2009; Young et al. 2010). However, that scheme assumes that the underlying power source is radioactive decay to separate SLSN-R from other SLSN-I. Here, we have shown that a model powered purely by cobalt decay cannot match the colors or the late-time observations: PISN models are considerably redder than what is observed for PS1-14bj past peak, and predict a very different late-time spectrum than what we observe. We note that PS1-14bj at least demonstrates that there exist SLSNe with the long rise times predicted by pair-instability models, which has not been observed before. By extension, it is possible that SN 2007bi may also have had a long rise-time.

A simple magnetar model can reproduce the long time scales by a combination of lower magnetic field and larger ejecta mass than is typically used to fit SLSNe. However, this model has the same problem as the Ni-powered model in explaining the near-constant rather than reddening color past peak, and generally overpredicts the late-time luminosity ($\gtrsim$ 150 days past peak). Both of these shortcomings could be overcome by relaxing the assumption that all the radiation from the magnetar is being thermalized in the ejecta; in this scenario the late time heating would be due to emission from the pulsar wind nebula breaking out, and the [O III] lines similarly coming from inner parts of the ejecta being ionized by the central source.

Alternatively, the persistent blue continuum and [O III] lines could arise from material being shocked and ionized by interaction with a CSM shell. Such lines are often seen in core-collapse SNe with CSM interaction, though typically at later phases than we observe here. This scenario could be distinguished from the magnetar breakout by continued spectral monitoring as the line velocities are expected to decrease in the CSM scenario, and stay constant or even increase in the magnetar case. X-ray or radio observations are another possibility.

PS1-14bj further demonstrates the need to explore hybrid models that combine multiple power sources contributing at different points in the light curve (e.g., Chatzopoulos et al. 2012). For example, Yan et al. (2015) proposed that interaction with CSM shells emitted during the pulsational pair instability (Woosley et al. 2007) could explain the late-time H emission of iPTF13ehe. Our discovery of emerging [O III] features in the late-time spectrum further demonstrates the potential of late-time monitoring in revealing the nature of SLSNe. The discovery of a second SLSN, LSQ14an, with late-time features similar to PS1-14bj in its spectrum shows that they are not unique, and may not be rare in slowly-evolving SLSNe.

vard University. This research has made use of NASA's Astrophysics Data System.

Facilities: PS1, MMT, Magellan:Baade, Magellan:Clay, Gemini:Gillett, Gemini:South, LBT, McGraw-Hill, Hiltner

REFERENCES

Alard, C., & Lupton, R. H. 1998, ApJ, 503, 325
Arnett, W. D. 1982, ApJ, 253, 785
Barkat, Z., Rakavy, G., & Sack, N. 1967, Physical Review Letters, 18, 379
Ben-Ami, S., Gal-Yam, A., Mazzali, P. A., et al. 2014, ApJ, 785, 37
Chatzopoulos, E., & Wheeler, J. C. 2012a, ApJ, 748, 42
—. 2012b, ApJ, 760, 154
Chatzopoulos, E., Wheeler, J. C., & Vinko, J. 2009, ApJ, 704, 1251
—. 2012, ApJ, 746, 121
Chatzopoulos, E., Wheeler, J. C., Vinko, J., Horvath, Z. L., & Nagy, A. 2013, ApJ, 773, 76
Chen, T.-W. 2015, PhD thesis, Queen's University Belfast
Chen, T.-W., Smartt, S. J., Jerkstrand, A., et al. 2015, MNRAS, 452, 1567
Chevalier, R. A., & Fransson, C. 1992, ApJ, 395, 540
—. 1994, ApJ, 420, 268
Chevalier, R. A., & Irwin, C. M. 2011, ApJ, 729, L6
Chomiuk, L., Chornock, R., Soderberg, A. M., et al. 2011, ApJ, 743, 114
Dessart, L., Audit, E., & Hillier, D. J. 2015, MNRAS, 449, 4304
Dessart, L., Hillier, D. J., Waldman, R., Livne, E., & Blondin, S. 2012, MNRAS, 426, L76
Dessart, L., Waldman, R., Livne, E., Hillier, D. J., & Blondin, S. 2013, MNRAS, 428, 3227
Dressler, A., Hare, T., Bigelow, B. C., & Osip, D. J. 2006, in Society of Photo-Optical Instrumentation Engineers (SPIE) Conference Series, Vol. 6269, Society of Photo-Optical Instrumentation Engineers (SPIE) Conference Series
Fesen, R. A., Gerardy, C. L., Filippenko, A. V., et al. 1999, AJ, 117, 725
Filippenko, A. V. 1982, PASP, 94, 715
Fransson, C. 1984, A&A, 132, 115
Fransson, C., Chevalier, R. A., Filippenko, A. V., et al. 2002, ApJ, 572, 350
Gal-Yam, A. 2012, Science, 337, 927
Gal-Yam, A., Mazzali, P., Ofek, E. O., et al. 2009, Nature, 462, 624
Garg, A., Stubbs, C. W., Challis, P., et al. 2007, AJ, 133, 403
Ginzburg, S., & Balberg, S. 2012, ApJ, 757, 178
Glazebrook, K., & Bland-Hawthorn, J. 2001, PASP, 113, 197
Hogg, D. W., Baldry, I. K., Blanton, M. R., & Eisenstein, D. J. 2002, ArXiv Astrophysics e-prints, astro-ph/0210394
Hook, I. M., Jørgensen, I., Allington-Smith, J. R., et al. 2004, PASP, 116, 425
Inserra, C., Smartt, S. J., Jerkstrand, A., et al. 2013, ApJ, 770, 128
Jerkstrand, A., Smartt, S. J., & Heger, A. 2016, MNRAS, 455, 3207
Kaiser, N., Burgett, W., Chambers, K., et al. 2010, in Society of Photo-Optical Instrumentation Engineers (SPIE) Conference Series, Vol. 7733, Society of Photo-Optical Instrumentation Engineers (SPIE) Conference Series
Kasen, D., & Bildsten, L. 2010, ApJ, 717, 245
Kasen, D., Woosley, S. E., & Heger, A. 2011, ApJ, 734, 102
Kennicutt, Jr., R. C. 1998, ARA&A, 36, 189
Komatsu, E., Smith, K. M., Dunkley, J., et al. 2011, ApJS, 192, 18
Kozyreva, A., Blinnikov, S., Langer, N., & Yoon, S.-C. 2014, A&A, 565, A70
Kriek, M., van Dokkum, P. G., Labbé, I., et al. 2009, ApJ, 700, 221
Leget, P.-F., Guillou, L. L., Fleury, M., et al. 2014, The Astronomer's Telegram, 5718, 1
Lunnan, R., Chornock, R., Berger, E., et al. 2013, ApJ, 771, 97
—. 2014, ApJ, 787, 138
Magnier, E. 2006, in The Advanced Maui Optical and Space Surveillance Technologies Conference
Magnier, E. A., Liu, M., Monet, D. G., & Chambers, K. C. 2008, in IAU Symposium, Vol. 248, IAU Symposium, ed. W. J. Jin, I. Platais, & M. A. C. Perryman, 553–559
Marchant, P., Langer, N., Podsiadlowski, P., Tauris, T. M., & Moriya, T. J. 2016, A&A, 588, A50
Margutti, R., Kamble, A., Milisavljevic, D., et al. 2016, ArXiv e-prints, arXiv:1601.06806
Mazzali, P. A., Sullivan, M., Pian, E., Greiner, J., & Kann, D. A. 2016, MNRAS, 458, 3455
McCrum, M., Smartt, S. J., Kotak, R., et al. 2014, MNRAS, 437, 656
Miknaitis, G., Pignata, G., Rest, A., et al. 2007, ApJ, 666, 674
Milisavljevic, D., & Fesen, R. A. 2008, ApJ, 677, 306
Milisavljevic, D., Fesen, R. A., Chevalier, R. A., et al. 2012, ApJ, 751, 25
Milisavljevic, D., Margutti, R., Kamble, A., et al. 2015, ApJ, 815, 120
Miller, A. A., Silverman, J. M., Butler, N. R., et al. 2010, MNRAS, 404, 305
Morgan, C. W., Byard, P. L., DePoy, D. L., et al. 2005, AJ, 129, 2504
Moriya, T., Tominaga, N., Tanaka, M., Maeda, K., & Nomoto, K. 2010, ApJ, 717, L83
Moriya, T. J., Blinnikov, S. I., Tominaga, N., et al. 2013, MNRAS, 428, 1020
Moriya, T. J., & Maeda, K. 2012, ApJ, 756, L22
Nicholl, M., & Smartt, S. J. 2016, MNRAS, 457, L79
Nicholl, M., Smartt, S. J., Jerkstrand, A., et al. 2013, Nature, 502, 346
—. 2014, MNRAS, 444, 2096
—. 2015, ApJ, 807, L18
Nicholl, M., Berger, E., Smartt, S. J., et al. 2016, ArXiv e-prints, arXiv:1603.04748
Ofek, E. O., Cameron, P. B., Kasliwal, M. M., et al. 2007, ApJ, 659, L13
Persson, S. E., Barkhouser, R., Birk, C., et al. 2008, in Society of Photo-Optical Instrumentation Engineers (SPIE) Conference Series, Vol. 7014, Society of Photo-Optical Instrumentation Engineers (SPIE) Conference Series
Quimby, R. M., Kulkarni, S. R., Kasliwal, M. M., et al. 2011, Nature, 474, 487
Rest, A., Stubbs, C., Becker, A. C., et al. 2005, ApJ, 634, 1103
Rest, A., Foley, R. J., Gezari, S., et al. 2011, ApJ, 729, 88
Rest, A., Scolnic, D., Foley, R. J., et al. 2014, ApJ, 795, 44
Schlafly, E. F., & Finkbeiner, D. P. 2011, ApJ, 737, 103
Schmidt, G. D., Weymann, R. J., & Foltz, C. B. 1989, PASP, 101, 713
Smartt, S. J., Valenti, S., Fraser, M., et al. 2015, A&A, 579, A40
Smith, N., Chornock, R., Silverman, J. M., Filippenko, A. V., & Foley, R. J. 2010, ApJ, 709, 856
Smith, N., Li, W., Foley, R. J., et al. 2007, ApJ, 666, 1116
Speziali, R., Di Paola, A., Giallongo, E., et al. 2008, in Proc. SPIE, Vol. 7014, Ground-based and Airborne Instrumentation for Astronomy II, 70144T
Thomas, R. C., Nugent, P. E., & Meza, J. C. 2011, PASP, 123, 237
Tonry, J., & Onaka, P. 2009, in Advanced Maui Optical and Space Surveillance Technologies Conference,
Tonry, J. L., Stubbs, C. W., Lykke, K. R., et al. 2012, ApJ, 750, 99
Valenti, S., Benetti, S., Cappellaro, E., et al. 2008, MNRAS, 383, 1485
Wang, S. Q., Wang, L. J., Dai, Z. G., & Wu, X. F. 2015, ApJ, 799, 107
Wheeler, J. C., Johnson, V., & Clocchiatti, A. 2015, MNRAS, 450, 1295
Woosley, S. E. 2010, ApJ, 719, L204
Woosley, S. E., Blinnikov, S., & Heger, A. 2007, Nature, 450, 390
Yan, L., Quimby, R., Ofek, E., et al. 2015, ApJ, 814, 108
Young, D. R., Smartt, S. J., Valenti, S., et al. 2010, A&A, 512, A70
Yusof, N., Hirschi, R., Meynet, G., et al. 2013, MNRAS, 433, 1114

Table 1
PS1-14bj Photometry

MJD (days)	Rest-frame Phase (days)	Filter	AB Mag	Instrument
56709.3	−60.5	$g_{\rm P1}$	22.70 ± 0.40	PS1
56751.2	−32.9	g	22.34 ± 0.06	MMT
56774.3	−17.7	g	22.43 ± 0.03	GN
56775.3	−17.1	g	22.59 ± 0.03	GN
56836.0	22.8	g	22.52 ± 0.03	LDSS
56952.5	99.4	g	22.97 ± 0.05	LBT
56981.4	118.4	g	23.17 ± 0.05	MMT
56993.5	126.3	g	23.29 ± 0.05	MMT
57038.2	155.7	g	23.45 ± 0.06	IMACS
57071.9	177.8	g	23.66 ± 0.08	IMACS
57109.3	202.4	g	24.16 ± 0.15	GN
57135.0	219.4	g	24.00 ± 0.10	IMACS
57158.0	234.5	g	24.06 ± 0.11	IMACS
56636.6	−108.2	$r_{\rm P1}$	23.25 ± 0.32	PS1
56666.6	−88.5	$r_{\rm P1}$	22.83 ± 0.26	PS1
56682.6	−78.0	$r_{\rm P1}$	22.39 ± 0.11	PS1
56744.3	−37.4	r	21.58 ± 0.02	GN
56751.2	−32.9	r	21.50 ± 0.03	MMT
56774.3	−17.7	r	21.50 ± 0.02	GN
56775.3	−17.1	r	21.54 ± 0.03	GN
56794.2	−4.7	r	21.47 ± 0.03	MMT
56807.1	3.8	r	21.48 ± 0.03	MMT
56833.0	20.8	r	21.53 ± 0.02	LDSS
56952.5	99.4	r	22.18 ± 0.03	LBT
56955.5	101.4	r	22.31 ± 0.06	MDM
56981.5	118.4	r	22.52 ± 0.04	MMT
56993.4	126.3	r	22.57 ± 0.04	MMT
57007.3	135.4	r	22.60 ± 0.05	IMACS
57038.2	155.7	r	22.74 ± 0.04	IMACS
57071.9	177.8	r	22.89 ± 0.06	IMACS
57109.3	202.4	r	23.08 ± 0.05	GN
57135.1	219.4	r	23.23 ± 0.10	IMACS
57157.0	233.8	r	23.31 ± 0.06	IMACS
57371.4	374.7	r	24.72 ± 0.20	IMACS
57396.3	391.0	r	24.45 ± 0.14	IMACS
57431.2	414.0	r	24.53 ± 0.17	IMACS
56656.6	−95.1	$i_{\rm P1}$	22.70 ± 0.17	PS1
56661.6	−91.8	$i_{\rm P1}$	22.52 ± 0.11	PS1
56668.5	−87.3	$i_{\rm P1}$	22.42 ± 0.21	PS1
56683.6	−77.4	$i_{\rm P1}$	22.01 ± 0.08	PS1
56744.3	−37.4	i	21.35 ± 0.02	GN
56751.2	−32.9	i	21.34 ± 0.02	MMT
56774.3	−17.7	i	21.35 ± 0.02	GN
56775.3	−17.1	i	21.28 ± 0.02	GN
56807.2	3.8	i	21.19 ± 0.02	MMT
56833.0	20.8	i	21.37 ± 0.02	LDSS
56952.5	99.4	i	22.14 ± 0.03	LBT
56981.5	118.4	i	22.37 ± 0.05	MMT
56993.4	126.3	i	22.35 ± 0.05	MMT
57007.3	135.4	i	22.47 ± 0.03	IMACS
57038.3	155.7	i	22.79 ± 0.04	IMACS
57071.9	177.8	i	22.85 ± 0.08	IMACS
57109.3	202.4	i	22.92 ± 0.06	GN
57129.1	215.5	i	23.05 ± 0.05	MDM
57131.2	216.9	i	23.21 ± 0.10	MMT
57135.1	219.4	i	23.16 ± 0.08	IMACS
57157.0	233.8	i	23.41 ± 0.10	IMACS
57371.3	374.6	i	24.24 ± 0.15	IMACS
57396.3	391.0	i	24.12 ± 0.12	IMACS
57431.2	414.0	i	24.48 ± 0.20	IMACS
56618.6	−120.1	$z_{\rm P1}$	23.53 ± 0.53	PS1
56629.6	−112.8	$z_{\rm P1}$	22.69 ± 0.27	PS1
56632.6	−110.9	$z_{\rm P1}$	22.78 ± 0.25	PS1
56637.6	−107.6	$z_{\rm P1}$	23.03 ± 0.44	PS1
56662.6	−91.2	$z_{\rm P1}$	22.17 ± 0.21	PS1
56667.7	−87.8	$z_{\rm P1}$	22.08 ± 0.21	PS1
56681.5	−78.7	$z_{\rm P1}$	22.24 ± 0.19	PS1
56774.3	−17.7	z	21.71 ± 0.04	GN
56775.3	−17.1	z	21.78 ± 0.05	GN
56833.0	20.8	z	21.64 ± 0.06	LDSS
56952.5	99.4	z	22.60 ± 0.09	LBT
57009.3	136.7	z	22.99 ± 0.10	IMACS
57039.3	156.4	z	23.16 ± 0.11	IMACS
57071.9	177.8	z	23.26 ± 0.13	IMACS
57135.1	219.4	z	24.00 ± 0.24	IMACS
57157.0	233.8	z	24.16 ± 0.27	IMACS
56757.0	-29.1	J	21.56 ± 0.10	FourStar
57111.1	203.6	J	23.24 ± 0.15	FourStar

Table 2
Log of PS1-14bj Spectroscopic Observations

UT Date	Phase[a] (days)	Instrument	Grating	Filter	Wavelength Range (Å)	Resolution (Å)	Exposure Time (s)	Mean Airmass
2014 Mar 08.32	−50.6	BlueChannel	300GPM	None	3330−8550	5.6	3600	1.21
2014 Mar 28.36	−37.4	GMOS-N	R400	OG515	5640−9910	7.1	3600	1.06
2014 Apr 27.34	−17.7	GMOS-N	R400	OG515	5485−9750	7.1	2435	1.26
2014 Apr 28.28	−17.1	GMOS-N	R400	OG515	5485−9750	7.1	1800	1.07
2014 Apr 28.20	−17.2	BlueChannel	300GPM	None	3330−8540	7.6	8000	1.29
2014 May 03.99	−13.4	GMOS-S	B600	None	3600−6430	4.6	3600	1.21
2014 Jun 25.99	+21.5	LDSS3C	VPH-All	None	4000−10000	8.1	1500	1.84
2014 Jun 27.99	+22.8	LDSS3C	VPH-Red	OG590	5925−10600	4.9	3600	2.01
2014 Dec 19.30	+137.4	IMACS	200/+15	None	4500−10000	7.1	7200	1.33
2015 Jan 15.27	+155.1	IMACS	300/+17.5	None	4200−9445	4.1	3600	1.21
2015 Mar 28.32	+202.4	GMOS-N	R400	OG515	5980−10315	7.1	7200	1.06

[a] Phase is in rest-frame days relative to bolometric maximum light.

Table 3
Log of LSQ14an Spectroscopic Observations

UT Date	Instrument	Grating	Filter	Wavelength Range (Å)	Resolution (Å)	Exposure Time (s)	Mean Airmass
2014 Jan 08.336	IMACS	300/+17.5	None	3700−9450	4.9	2400	1.17
2014 Feb 28.375	IMACS	300/+17.5	None	3700−10300	3.6	1800	1.11
2014 Jun 25.034	LDSS3C	VPH-All	None	4000−10000	8.1	3000	1.06
2015 Feb 19.254	IMACS	300/+17.5	None	3700−9460	4.9	1800	1.08
2015 Apr 23.300	IMACS	300/+17.5	None	3700−9435	4.9	3000	1.49
2015 Jul 17.041	LDSS3C	VPH-All	None	4000−10000	8.1	3600	1.25

Table 4
PS1-14bj Bolometric Light Curve

Phase (rest frame days)	Luminosity (10^{43} erg s^{-1})
−120.1	0.64 ± 0.37
−112.8	1.40 ± 0.55
−110.9	1.29 ± 0.49
−107.6	1.02 ± 0.52
−91.2	2.26 ± 0.81
−88.5	2.45 ± 0.55
−78.0	2.10 ± 0.27
−37.4	4.21 ± 0.12
−32.9	4.34 ± 0.13
−17.7	4.41 ± 0.10
−17.1	4.29 ± 0.11
−4.7	4.54 ± 0.13
3.8	4.56 ± 0.14
20.8	4.50 ± 0.14
99.4	2.15 ± 0.09
101.4	2.21 ± 0.08
118.4	1.79 ± 0.08
126.3	1.67 ± 0.07
135.4	1.57 ± 0.05
155.7	1.28 ± 0.06
177.8	1.14 ± 0.08
202.4	0.80 ± 0.06
219.4	0.73 ± 0.07
233.8	0.64 ± 0.07
374.7	0.23 ± 0.07
391.0	0.27 ± 0.06
414.0	0.22 ± 0.06